

Ultrafast On-Chip Online Learning via Spline Locality in Kolmogorov–Arnold Networks

Duc Hoang ^{*1} Aarush Gupta ^{*1} Philip Harris ¹

Abstract

Ultrafast online learning is essential for high-frequency systems, such as controls for quantum computing and nuclear fusion, where adaptation must occur on sub-microsecond timescales. Meeting these requirements demands low-latency, fixed-precision computation under strict memory constraints, a regime in which conventional Multi-Layer Perceptrons (MLPs) are both inefficient and numerically unstable. We identify key properties of Kolmogorov–Arnold Networks (KANs) that align with these constraints. Specifically, we show that: (i) KAN updates exploiting B-spline locality are sparse, enabling superior on-chip resource scaling, and (ii) KANs are inherently robust to fixed-point quantization. By implementing fixed-point online training on Field-Programmable Gate Arrays (FPGAs), a representative platform for on-chip computation, we demonstrate that KAN-based online learners are significantly more efficient and expressive than MLPs across a range of low-latency and resource-constrained tasks. To our knowledge, this work is the first to demonstrate model-free online learning at sub-microsecond latencies.

 Duchstf/ECLAIR

1. Introduction

Ultrafast **model-free online learning**, where the network learns an input-output mapping directly from streaming data without assuming an explicit system model, is essential in domains with high-frequency, non-stationary dynamics. These include quantum control, high-speed communications, and plasma diagnostics, where adaptation must occur on sub-microsecond timescales (Berritta et al., 2024). In these regimes, host–accelerator training loops are too slow:

^{*}Equal contribution ¹MIT. Correspondence to: Duc Hoang <dhoang@mit.edu>.

Preprint. February 3, 2026.

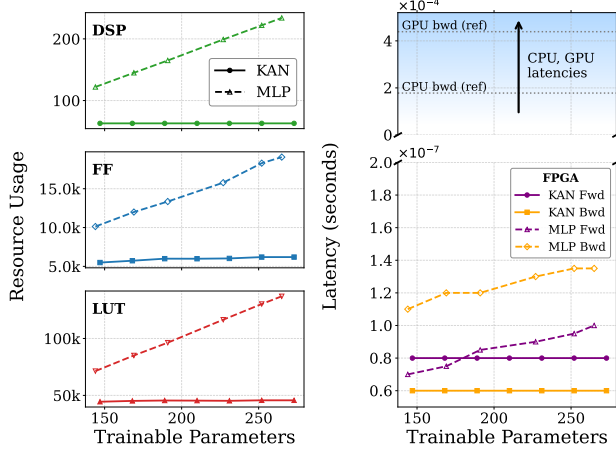


Figure 1. Hardware scaling under ultrafast on-chip online learning. On a non-stationary qubit readout task with fixed-point training, MLPs grow roughly linearly in on-chip resources (DSP/FF/LUT) and in forward/backward latency with parameter count. KANs leverage B-spline locality and favorable approximation scaling, increasing capacity (via grid size G) with near-constant resources and sub-100 ns latency. CPU/GPU (A100) lines show reference latencies for PyTorch implementations.

by the time gradients are computed off-chip and parameters return over high-latency links (e.g. PCIe), the system may have already shifted operating conditions. Real-time adaptation, therefore, *requires* both inference and training to be performed directly on-chip, with low-latency, fixed-precision computation under strict memory constraints.

Currently, end-to-end on-chip training with standard MLPs remains impractical. Backpropagation is expensive, and reduced precision can destabilize gradient-based optimization (Yan et al., 2024). As a result, prior systems focused on either hyperspecialized training workflows (Tang et al., 2022) or a decoupling of learning from inference, even when continuous adaptation is required (Sivak et al., 2025). This motivates a fundamental architectural question: *what model properties make fixed-point, low-latency, on-chip online updates both stable and hardware-efficient?*

We revisit **Kolmogorov–Arnold Networks (KANs)** (Liu et al., 2025) from a hardware-centric perspective, where their perceived inefficiency (Tran et al., 2024; Hou et al.,

2025) largely reflects assumptions about batched, floating-point training and inference on GPUs. In contrast, custom hardware can exploit KANs’ locally supported activations and sparse gradient updates, mitigating the global error propagation and dense compute overhead of MLPs.

Guided by theory on per-sample update cost and approximation error, we realize an efficient and ultrafast implementation of KAN on custom hardware (FPGA). Under equal parameter budgets and identical precision constraints, KANs achieve superior numerical stability, lower update cost, and ultrafast latency. This enables reliable gradient updates on streaming data, supporting model-free online learning at sub-microsecond timescales for the first time.

2. Related Works

Application Domains. Ultra low-latency online adaptation is critical in domains where system dynamics evolve on microsecond or nanosecond timescales, including plasma control (Wei et al., 2024), optical and wireless communications (Wang et al., 2018), quantum control (Reuer et al., 2023; Guglielmo et al., 2025; Liyanage et al., 2024), and particle accelerator tuning (Scheinker, 2021). Most existing approaches rely on meta-learning (Nagabandi et al., 2019) or heterogeneous host–device pipelines, in which learning occurs off-device and models are periodically redeployed (Sivak et al., 2025). Such workflows incur communication and scheduling latency and cannot support deterministic, sub-microsecond adaptation. As a result, while custom hardware is widely used for real-time control (Beritta et al., 2024) and inference (Guglielmo et al., 2025), learning is typically absent or limited to primitive update rules (Jones et al., 2025).

On-Device Training. On-device neural network inference is well established across custom and embedded hardware platforms (e.g. HLS4ML (Fahim et al., 2021), FINN (Blott et al., 2018)), but fully on-device training remains largely unexplored. Prior work focuses on accelerating batch training (Dey et al., 2018; Luo et al., 2019) or targets narrow, task-specific scenarios (Liu et al., 2023; Gadea et al., 2000), rather than continuous online adaptation. Backpropagation fundamentally limits this regime by increasing arithmetic workload, requiring dense activation storage, and amplifying numerical instability under reduced precision (Tang et al., 2022; Yan et al., 2024). Existing architectural and compiler-level optimizations mitigate only specific bottlenecks (Zhang et al., 2021; Venkataramanaiah et al., 2019; Kara et al., 2017). Consequently, despite the dominance of MLPs driven by the “hardware lottery” (Hooker, 2020), current approaches remain unsuitable for stable, deterministic on-chip online learning under tight latency and precision constraints.

KANs and Perceived Hardware Limitations. KANs (Liu et al., 2025) use learnable spline activations and perform well empirically, yet are often labeled hardware-impractical due to recursive spline evaluation and increased per-edge parameterization (Tran et al., 2024; Hou et al., 2025). However, these prevailing critiques of KAN hardware inefficiency are GPU-centric or inference-focused and overlook the locality and sparsity induced by B-spline activations. Prior hardware work targets analog hardware (Duarte et al., 2025) or LUT-based inference (Hoang et al., 2025; Huang et al., 2025), but does not address training. To our knowledge, fully on-chip KAN training with deterministic execution, fixed-point arithmetic, and bounded local memory has not been analyzed or demonstrated, leaving the question of whether KANs can support hardware-efficient on-device learning entirely open.

Other Adaptive Methods. Online adaptation includes statistical estimators and specialized learners (e.g. Kalman/LMS filters, ELMs, RBF, sparse-coding models, and SNNs) that can run at low latency on hardware (Babu & Parthasarathy, 2022; Johnson et al., 2024; Zang et al., 2025; Le et al., 2017; Borrageiro et al., 2022; Mehrabi et al., 2024). However, these methods either assume restricted model classes (e.g. linear/Gaussian), rely on fixed/random feature maps (e.g. ELM/RBF), or require non-standard training pipelines with non-deterministic timing (e.g. SNNs). These properties make them unsuitable baselines for *model-free, gradient-based* online learning with *deterministic* sub- μ s updates. Moreover, prior studies focus on inference or task-specific update rules rather than end-to-end training pipelines.

3. Theoretical Motivations

3.1. Notation and Preliminaries

Setting. We compare dense MLPs and KANs under an identical parameter budget N and uniform fixed-point quantization with step size Δ .

Notation. An MLP layer ℓ is $\Phi_\ell(x) = \sigma(W_\ell x + b_\ell)$ with $W_\ell \in \mathbb{R}^{d_{\text{out}} \times d_{\text{in}}}$ and $N_{\text{MLP}} \approx d_{\text{in}}d_{\text{out}}$. A KAN layer ℓ applies learnable univariate spline maps on edges:

$$x_{\ell+1,j} = \sum_{i=1}^{n_\ell} \phi_{\ell,j,i}(x_{\ell,i}), \quad \phi_{\ell,j,i}(x) = \sum_{g=1}^G w_{\ell,j,i,g} B_g(x),$$

where $\{B_g\}_{g=1}^G$ are p -th order B-spline basis functions on a grid of size G , giving $N_{\text{KAN}} = d_{\text{in}}d_{\text{out}}(G + p + 1)$. Throughout, we enforce $N_{\text{MLP}} = N_{\text{KAN}} = N$.

Definition 3.1 (Saturated fixed-point quantization). For $\Delta, R > 0$, define the quantization function as:

$$Q_\Delta(z) = \left[\Delta \cdot \text{round} \left(\frac{z}{\Delta} \right) \right]_{-R}^R$$

where $[x]_a^b = \min(b, \max(a, x))$ denotes the clipping operation. Bitwidths are quoted in terms of the total precision W , and the integer precision I , often as $\langle W, I \rangle$.

3.2. B-Spline Locality Enables Sparse Updates

The computational advantage of KANs for on-chip learning stems from B-spline basis functions having local support.

Lemma 3.2 (Local support of B-splines (Liu et al., 2025)). *For spline order p , each basis function B_g has local support. For any input coordinate x_i , at most $s = p + 1$ indices g satisfy $B_g(x_i) \neq 0$.*

This locality directly reduces per-sample update cost:

Theorem 3.3 (Update complexity reduction). *Let $\mathcal{C}_{\text{update}}(\cdot)$ denote the number of scalar arithmetic operations required to compute parameter gradients for one sample. Under an equal parameter budget N ,*

$$\mathcal{C}_{\text{update}}(\text{KAN}) = \frac{s}{G + s} \mathcal{C}_{\text{update}}(\text{MLP}).$$

The proof appears in Appendix A.1. The key insight is that while MLPs produce dense gradients over all N parameters, KANs update only the $O(s)$ active coefficients per edge, **independent of total capacity N** .

3.3. Capacity Scaling at Constant Compute

Theorem 3.3 has a powerful implication for capacity scaling. KAN approximation quality improves with grid resolution: for sufficiently smooth targets and $0 \leq m \leq k$, there exist spline maps on a grid of size G such that (Liu et al., 2025)

$$\|f - f_G\|_{C^m} \leq C G^{-k-1+m}.$$

Crucially, increasing G adds *stored* coefficients but not *active* computation. By Lemma 3.2, each edge still reads and updates only $O(s)$ coefficients per sample. In contrast, scaling MLP capacity requires proportionally more MACs and gradient updates.

This decoupling also benefits continual learning: because each sample modifies only coefficients in a local region of the input space, updates preserve prior fits elsewhere, reducing catastrophic forgetting compared to dense MLP gradients.

Hardware Takeaway On custom hardware, per-sample latency and memory bandwidth scale with the size of the *active* coefficient set s , not total parameters N . KANs thus expose a clean capacity knob: scaling the grid size G improves approximation capabilities while per-sample compute remains essentially constant. The main cost is extra coefficient storage (memory depth), a favorable trade-off on-chip (LUT/FF/BRAM) that typically adds little overhead compared to arithmetic compute on custom hardware.

3.4. Robustness to Fixed-Point Quantization

KANs possess properties that make them more robust to fixed-point quantization noise as compared to MLPs.

Theorem 3.4 (KAN Activation Bounds). *Consider a KAN activation $\phi(x) = \sum_g W_g B_g(x)$. Then, for any input x ,*

$$\min_i W_i \leq \phi(x) \leq \max_i W_i.$$

This theorem is proven in Appendix A.2.

Remark. Unlike MLPs, where outputs scale with inputs via multiplication, KAN activations are convex combinations of learned coefficients, which are bounded and stable regardless of input magnitude. For a given input range, B-spline functions also tend to produce outputs that are uniformly distributed in magnitude. This inherent *magnitude normalization* in KANs is essential for stability under fixed-point quantization, where representing wide dynamic ranges is challenging.

Theorem 3.5 (Bounded Gradient Sensitivity). *Consider a single layer ℓ under quantization Q_Δ (Definition 3.1), and let $\delta_{\ell+1,j} = \frac{\partial \mathcal{L}}{\partial x_{\ell+1,j}}$ denote the backpropagated error signal.*

MLP. *The weight gradient satisfies*

$$\frac{\partial \mathcal{L}}{\partial W_{\ell,ji}} = \delta_{\ell+1,j} \cdot x_{\ell,i},$$

scaling linearly with input magnitude $|x_{\ell,i}|$.

KAN. *The coefficient gradient satisfies*

$$\frac{\partial \mathcal{L}}{\partial w_{\ell,j,i,g}} = \delta_{\ell+1,j} \cdot B_g(x_{\ell,i}),$$

where $B_g(x) \in [0, 1]$ by the B-spline partition of unity.

Consequently, for quantization-induced gradient error ϵ ,

$$\text{Var}[\epsilon_{\text{MLP}}] = O(\Delta^2 \text{Var}[x_\ell]), \quad \text{Var}[\epsilon_{\text{KAN}}] = O(\Delta^2),$$

where the KAN bound is independent of input statistics.

The proof for this theorem is provided in Appendix A.3.

Remark. While Theorem 3.4 bounds *forward* activations within the coefficient range, this theorem bounds *backward* gradients within the B-spline envelope. Together, they ensure that both forward and backward passes remain numerically stable under aggressive fixed-point quantization, a critical property for resource-constrained on-chip implementations where wide dynamic range is impractical.

4. Custom Hardware Implementation

Figure 2 contrasts our custom FPGA training kernels for KAN and MLP under identical streaming I/O, fixed-point

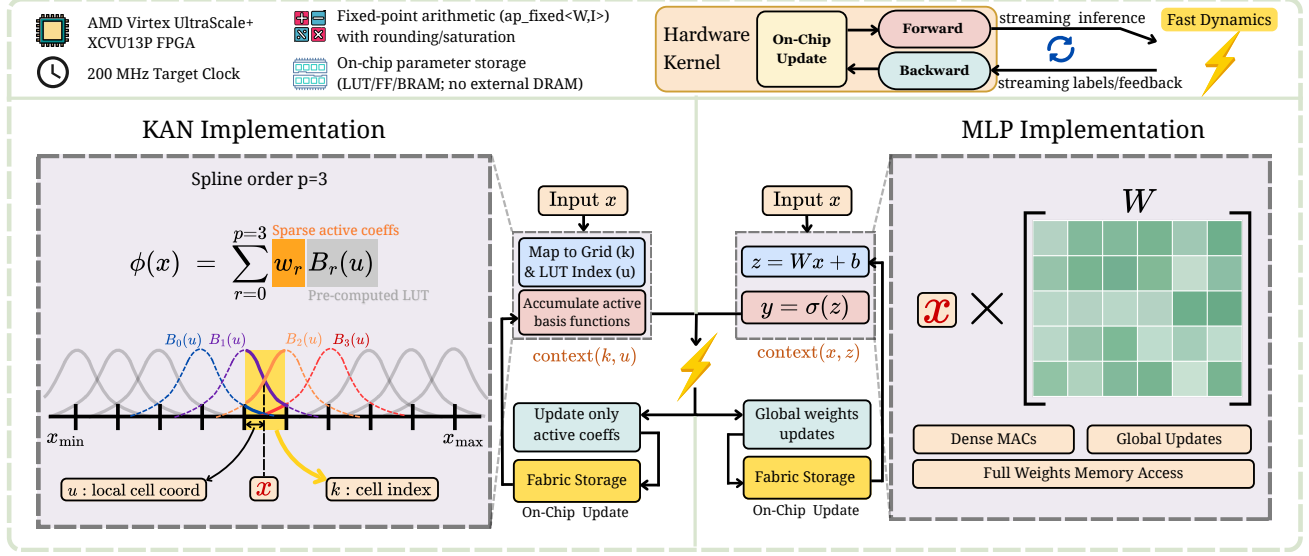


Figure 2. Overview of our streaming custom hardware kernels for fully online learning. KAN (left) and MLP (right) are synthesized in Vitis HLS as single hardware kernels (200 MHz, AMD Virtex UltraScale+ XCVU13P) that process streaming inputs and perform forward inference, backward gradient propagation, and in-place on-chip parameter updates with deterministic latency. **KAN:** each input x is mapped to a grid cell index k and LUT index u ; only the $(p+1)$ active B-spline basis functions are read from a small ROM LUT and accumulated, and the cached (k, u) context is reused in backprop to update only active coefficients. Gradients are computed using B-spline derivatives stored in LUTs. **MLP:** layers compute $z = Wx + b$, $y = \sigma(z)$ with dense MACs and global weight/bias updates using cached pre-activations. LUTs and per-sample context buffers are fully partitioned, while trainable parameters reside entirely on-chip (LUTRAM/BRAM/FF depending on synthesis) with explicit array partitioning to expose parallel accesses (no external DRAM).

arithmetic, and fully on-chip state. Here we highlight only the key implementation choices. Full details are provided in Appendix B.

KAN framework exploiting locality. Prior KAN implementations are GPU-centric and typically evaluate B-splines via expensive de Boor’s recursion, which obscures and underutilizes local support. We instead exploit B-spline locality explicitly: spline basis values/derivatives are stored in small precomputed **ROM LUTs**, and training performs **index-driven updates of only the $(p+1)$ active coefficients** per edge. Then, per-sample bandwidth/compute scales with the active set rather than the full parameter tensor.

MLP baseline. The MLP uses the same streaming interface and update rule, but performs dense $Wx+b$ MACs and dense (global) weight/bias updates, with a small context buffer caching layer inputs and pre-activations.

5. Experiments

We evaluate our FPGA kernels in the target regime of real-time learning: batch-size-one updates, non-stationary streams, and fixed-point arithmetic with deterministic latency. We study three fully online benchmarks: drifting regression (sensor calibration drift), adaptive single-shot qubit readout, and non-stationary Acrobot control. We then analyze scalability in Section 6 on higher-dimensional digit classification with continuous angular drift.

5.1. Evaluation: Online learning under fixed-point

Online protocol. We adopt a standard online learning protocol (Nagabandi et al., 2019): at each time step t , the learner receives \mathbf{x}_t , produces \hat{y}_t , and performs a single update from the local feedback signal (supervised error or RL reward/advantage). To ensure model non-stationarity, we assume the stream is governed by an unobserved context τ_t that controls both the data distribution and the optimal decision rule, where it may drift stochastically or adversarially.

Models and baselines. We use MLPs as the primary baseline, since they are the dominant general-purpose function approximator and the architecture most directly comparable to KANs. More generally, the MLP baseline serves as a proxy for the broader class of non-local architectures (e.g. dense matrix multiplication layers). In each experiment, we compare KANs against two fixed-role MLP baselines: (i) **MLP-P**, parameter-matched to the KAN budget N , and (ii) **MLP-L**, a larger MLP scaled to match the KAN’s stable asymptotic performance. For Acrobot, we specify the online algorithm, Actor-Critic (Konda & Tsitsiklis, 1999) or DQN (Mnih et al., 2013), when relevant. For MLPs, we sweep depth/width and ReLU, Tanh, and SiLU activations, and report the best-performing design under the same online and numeric constraints. We focus on MLP baselines as they broadly encompass techniques such as LMS filters, ELMs, and related methods; temporal architectures like SNNs rep-

Table 1. Experimental configurations. All models use single-batch updates. Fixed-point formats follow Definition 3.1 and are reported as $\langle W, I \rangle$. Learning rates and architectures are grid-searched; ReLU outperforms Tanh/SiLU on hardware. Metric reports the task objective: cumulative regret (\downarrow) for regression, accuracy (\uparrow) for classification, and episodic return (\uparrow) for control.

Experiment	Model	Dimension	Activation	# Params	G	s	η	Bitwidth	Metric (\downarrow Reg / \uparrow Acc / \uparrow Ret)	Task
Adaptive Function Approximation	KAN	[1,1]	-	13	10	3	0.5	$\langle 6, 2 \rangle$	13.2	Regression
	MLP-P	[1,2,2,1]	ReLU	13	-	-	0.1	$\langle 6, 2 \rangle$	97.6	Regression
	MLP-L	[1,16,16,1]	ReLU	321	-	-	0.1	$\langle 6, 2 \rangle$	48.3	Regression
Single-Shot Qubit Readout	KAN	[2, 7, 1]	-	273	10	3	0.05	$\langle 7, 3 \rangle$	92.8%	Classification
	MLP-P	[2,20,8.5,1]	ReLU	279	-	-	0.01	$\langle 10, 3 \rangle$	69.8%	Classification
	MLP-L	[2,16,16,16,1]	ReLU	609	-	-	0.015	$\langle 10, 3 \rangle$	62.4%	Classification
Non-Stationary Acrobot Control	KAN-AC	[6,4]	-	144	5	1	1e-3	$\langle 22, 8 \rangle$	-104	Control (RL)
	MLP-AC-P	[6,13,4]	ReLU	147	-	-	3e-4	$\langle 22, 8 \rangle$	-500 (incl. float)	Control (RL)
	MLP-AC-L	[6,32,32,4]	ReLU	1412	-	-	1e-4	$\langle 22, 8 \rangle$	-500 (incl. float)	Control (RL)
	MLP-DQN	[6,128,128,3]	ReLU	17,795	-	-	1e-6	float	-298	Control (RL)

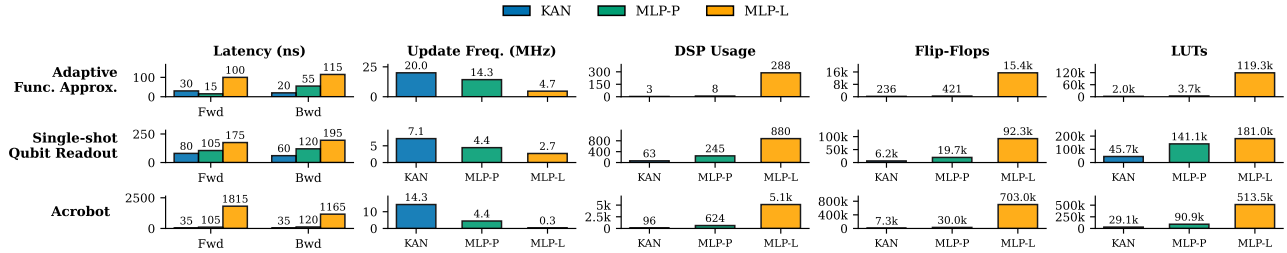


Figure 3. Post-synthesis FPGA latency and resource cost for fully online learning. Models are synthesized for an AMD VirtexTM UltraScale+TM XCVU13P at 200 MHz. Across tasks, KAN achieves the best latency-resource trade-off (DSP/FF/LUT) and the highest update rate (online updates/s, forward + backward). MLPs use more resources and/or diverge under fixed-point updates. No BRAM was used for either architecture across these experiments.

resent a distinct class of methods due to non-deterministic latency characteristics.

Metrics. We report task-appropriate online performance metrics: cumulative regret for drifting regression, running accuracy for qubit readout, and episodic return for control. We also report post-synthesis FPGA latency and resource utilization (LUTs/FFs/BRAMs/DSPs).

Hyperparameters. Architectures, learning rates, and fixed-point formats are summarized in Table 1.

5.2. Benchmark 1: Adaptive Function Approximation Under Concept Drift

We first consider a controlled non-stationary regression task as a proxy for real-time sensor calibration and signal recovery, where the underlying transfer function changes and must be tracked online.

Task. The task runs for $T = 1500$ steps. Inputs $x_t \sim \mathcal{U}[-1, 1]$ and targets follow a piecewise latent function with regime changes at $t = 500$ and $t = 1000$:

$$y_t = \begin{cases} \sin(x_t) + 0.3x_t^2 & 0 \leq t < 500 \\ -\cos(2x_t) + 0.1x_t^3 + 1.0 & 500 \leq t < 1000 \\ \exp(-0.5(x_t - 1)^2) + 0.05x_t^3 & 1000 \leq t < 1500 \end{cases}$$

Protocol and metric. Models are updated online with batch size 1 using a fixed learning rate η and the instantaneous gradient of the squared error. We report cumulative regret $R_T = \sum_{t=1}^T \text{MSE}_t$ to capture both convergence speed and adaptation after regime shifts.

Results. Figure 4 shows that in floating point, KAN achieves the lowest cumulative regret and re-adapts immediately after each regime change, while the parameter-matched MLP-P fails to track the drift and its regret grows steadily. A larger MLP-L can eventually recover, but adapts more slowly after shifts, yielding higher regret over the stream. Under fixed-point quantization (2 integer bits), KAN remains stable across total bitwidths, with only mild degradation at very low precision. In contrast, MLP-L exhibits a sharp precision cliff: low bitwidth leads to large final regret and high variance, and increasing bitwidth is required to regain stable learning. Figure 5 further shows that KAN benefits from increasing grid size G until reaching a quantization-limited floor set by bitwidth, whereas for MLPs, increasing parameter count N shows diminishing returns and amplifies sensitivity to quantization, destabilizing learning at low precision.

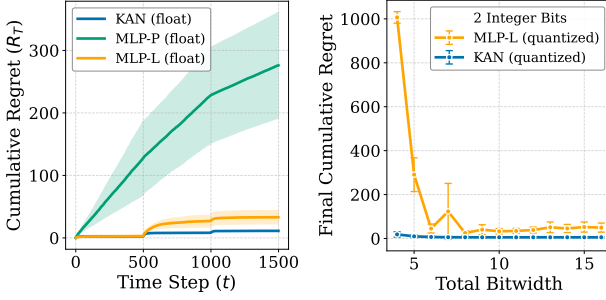


Figure 4. Adaptive function approximation under concept drift. **Left:** Cumulative regret with regime changes at $t = 500, 1000$: KAN adapts rapidly, MLP-P diverges, and MLP-L converges more slowly. **Right:** Final cumulative regret vs. fixed-point bitwidth (2 integer bits): KAN remains stable under quantization while MLP-L degrades at low precision.

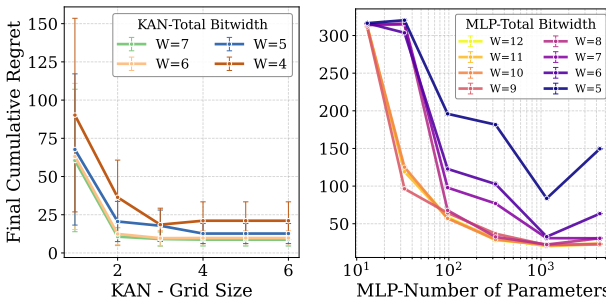


Figure 5. Empirical validation of approximation under quantization. **Left (KAN):** Error improves with grid size G until reaching a quantization floor set by bitwidth. **Right (MLP):** Increasing parameter count N amplifies sensitivity to quantization and destabilizes learning.

5.3. Benchmark 2: Adaptive Single-shot Qubit Readout

FPGAs are central to quantum computing platforms for deterministic, ultra-low-latency readout, feedback, and calibration (Guglielmo et al., 2025; Berritta et al., 2024). We cast single-shot qubit readout as an online binary classification problem with drifting, non-linearly separable decision boundaries.

Task. Each time step yields a noisy IQ sample $\mathbf{x}_t = (I_t, Q_t)$ from a rotating XOR constellation with Gaussian noise, Kerr-type phase distortion, and slow global drift. Full task details are provided in Appendix C.

Protocol and metric. Models are updated online from local label feedback at each step, with no buffering. We report the instantaneous accuracy and its running average over time.

Results. Figure 6 illustrates fully online running accuracy under drifting, non-linearly separable IQ constellations and visualizes the learned decision boundary at a representative time. Figure 7 sweeps capacity at fixed precision, KAN grid size G versus MLP parameter count N . KAN performance improves monotonically with larger G , whereas for MLPs

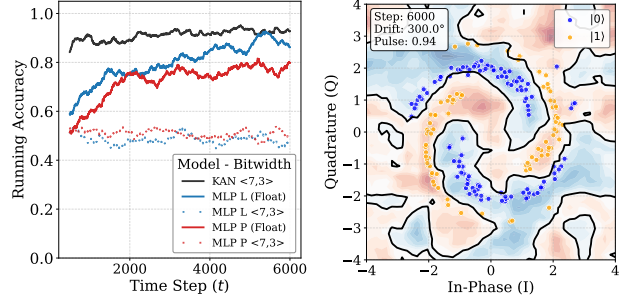


Figure 6. Adaptive single-shot qubit readout. **Left:** Online running accuracy. Quantized KAN tracks drift and avoids the collapse observed in quantized MLPs. **Right:** Snapshot of learned decision boundary at $t = 6000$: KAN tracks the drifting IQ distributions despite large phase drift.

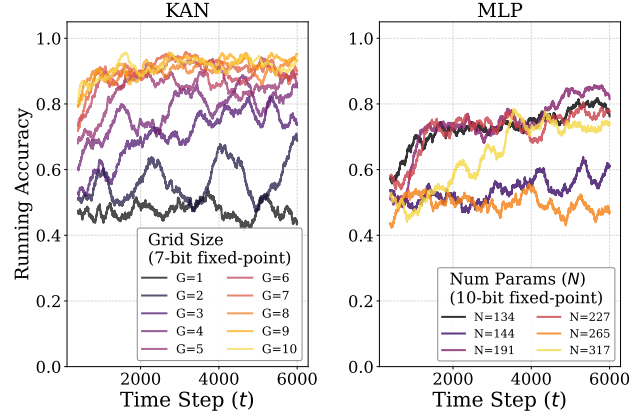


Figure 7. Capacity-precision decoupling under drift. **Left (KAN):** Accuracy improves monotonically with grid size G even under aggressive quantization. **Right (MLP):** Under 10-bit fixed-point training, increasing parameter count N yields only marginal accuracy gains and often destabilizes learning.

increasing N is the only scaling knob and often destabilizes convergence under fixed-bit arithmetic. Figure 1 quantifies how our synthesized fixed-point online training kernels scale with trainable parameters.

5.4. Benchmark 3: Online Policy Optimization under Non-stationary Dynamics

We evaluate the agent’s ability to adapt to non-stationary physical dynamics on Acrobot-v1 (Sutton, 1995).

Task. The agent observes a 6D state and selects one of three torques. To induce non-stationarity, we randomize the link masses ($m \in [0.8, 1.2]$) and lengths ($l \in [0.9, 1.1]$) at the start of every episode, requiring the agent to continually adjust its control policy.

Online actor-critic. We use an *online N-step actor-critic* update ($N=3$) with a shared network that outputs (i) action logits and (ii) a state-value estimate. At each step, we sample an action from the softmax policy and perform a

single batch update using an N -step bootstrapped return. This setting is deliberately stringent: non-stationary dynamics, stochastic exploration, and fully online updates amplify gradient interference in dense networks.

Baselines and metric. We compare (i) our fixed-point KAN policy/value network to (ii) MLP baselines (small/large, float) trained with *identical* online actor-critic rule, and (iii) a streaming value-learning baseline: online DQN-style Q-learning (ϵ -greedy, Huber TD loss) without replay. We report episodic return over time (mean \pm std over random seeds) and mark the environment’s solved threshold.

Results. As shown in Figure 8, under per-episode randomization, KAN sustains online improvement with fixed-point updates, while actor-critic MLPs are markedly less stable even in floating point. A larger MLP can recover only with the more stable value-learning update, supporting our claim that *update sparsity mitigates interference in non-stationary streams* (Lemma 3.2).

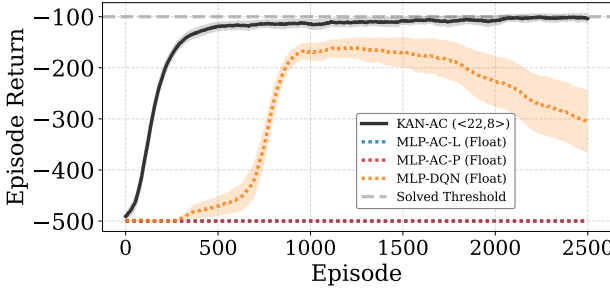


Figure 8. Non-stationary Acrobot control. Episodic return under randomized dynamics (link masses/lengths resampled each episode; mean \pm std over seeds). The fixed-point KAN actor-critic (black) reaches the solved regime in ~ 300 episodes and remains stable, while online actor-critic MLPs fail to adapt even at $10 \times$ the KAN parameter budget. An MLP only succeeds with a more stable online DQN update and a much larger network ($\sim 120 \times$), but learns more slowly and degrades under continued randomization.

5.5. Hardware results

We report post-synthesis FPGA latency and resource utilization for all models in Figure 3. B-spline locality yields sparse KAN updates, reducing DSP/FF/LUT usage and latency versus a parameter-matched MLP (Theorem 3.3), while keeping both forward and backward passes in the sub-100ns regime across all experiments.

6. Scalability

The preceding benchmarks already establish the key comparative conclusions against dense MLPs: (i) locality yields sparse per-sample updates and lower update cost (Lemma 3.2, Theorem 3.3), and (ii) capacity can be increased via grid resolution G without increasing the active

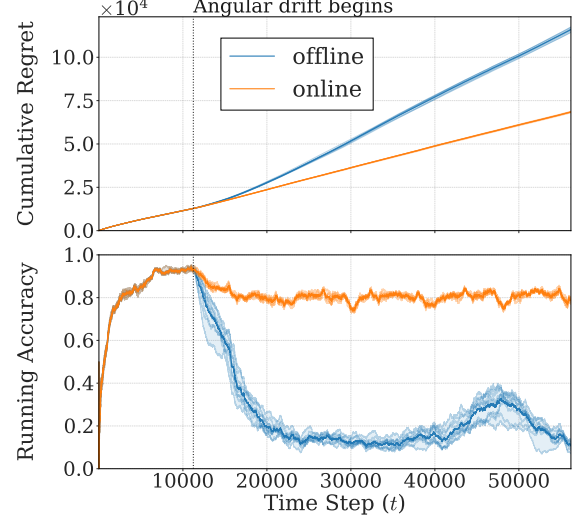


Figure 9. Comparison of online and offline learner performance on digit classification with angular drift. The online learner maintains an accuracy of 80% even with extreme angular drifts. In comparison, the frozen learner is only able to consistently classify around 20% of inputs correctly, with a cumulative regret over 50% that of the online learner.

compute per sample (Section 3.3), while maintaining stability under fixed-point updates (Theorems 3.4–3.5). In this section, we thus focus on the scaling properties of online KANs through higher-dimensional tasks.

6.1. Digit Classification with Online Drift

We take the classic problem of digit classification and introduce a constant *angular drift*, or rotation, over time. This drift is representative of many types of sensor degradations and distribution shifts that occur in real-time systems. By the final timestep, images have rotated nearly 230° , making rapid adaptation essential yet tricky for model-free online learners.

Task Setup. We use the UCI dataset containing 5,620 flattened 8x8 images of handwritten digits (Alpaydin & Kaynak, 1998). The online learner is initially fed in $N_{\text{stationary}} = 2$ epochs of images; after this, we train for $N_{\text{rotating}} = 8$ epochs where the image on step t is rotated by $\theta(t) = \omega t$, with $\omega = 0.005^\circ/\text{step}$.

Evaluation. To evaluate adaptation speed, we plot cumulative regret on the cross-entropy loss as well as running accuracy on the past 1,000 samples. To demonstrate the necessity of online learning, we compare to a baseline learner that does not update its parameters for the rotating epochs.

Results. Figure 9 demonstrates that the online learner is significantly more accurate and stable, demonstrating its ability to adapt to extreme distribution shifts when compared to a pretrained model.

6.2. Ablation Studies

We study scalability to higher-dimensional inputs by taking the architecture used for the digits task and scaling up input dimension, freezing all other hyperparameters. As shown in Figure 10, we maintain sub- μ s forward and backward passes even for models exceeding 10^5 trainable parameters. Because KAN layers are more expressive than MLPs, they typically require less depth to achieve comparable performance; paired with sparse, locality-driven gradient updates, this enables ultrafast backpropagation at scales difficult to attain with on-chip dense MLP training.

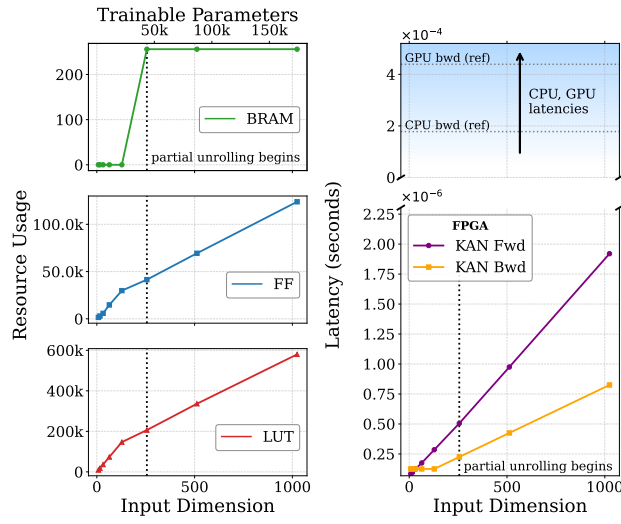


Figure 10. Resource and latency scaling estimates with increasing input dimension. Resource usage and latency scales roughly linearly with the input dimension and thus the trainable parameters. We partially unroll (reduce parallelism) for input dimensions greater than 256 to accommodate larger networks on the FPGA. Exact latency and resource values depend on specific implementation techniques, which can be tuned for the desired application.

7. Limitations

We use fully online, single batch SGD update to meet sub- μ s streaming constraints; this differs from common RL practice (e.g. PPO), which leverages trajectory batches and can converge faster. While our Acrobot setting is intentionally stringent (per-episode randomization and stochastic exploration), our kernels could be extended to accumulate gradients over short windows, trading latency and resources for stability while remaining streaming-friendly. More work also needs to be done in understanding how other optimizers (e.g. Adam) work under fixed-point learning dynamics for KAN and MLP architectures.

For a clean, hardware-faithful architectural comparison, we adopt a streamlined MLP baseline without auxiliary training features such as layer normalization or dropout. Although

effective in software, these mechanisms introduce nontrivial on-chip overhead and can blur effects attributable to architecture alone. This design isolates intrinsic learning behavior and fixed-point robustness of KANs versus MLPs. Future work can incorporate these enhancements and quantify the resulting accuracy–resource–latency trade-offs.

For scalability, the reported ablations assume a fixed set of hyperparameters; in other regimes, architectural choices may affect resource usage and latency, although we expect linear scaling trends to persist. For example, higher task complexity may necessitate increasing the spline order, which was previously held constant, to maintain sufficient representational capacity.

Additionally, while we utilize HLS to facilitate rapid prototyping, manual RTL refinement might offer better hardware efficiency. However, our focus remains on the architectural merits of KANs and order-of-magnitude estimates and comparisons, rather than extreme, low-level hardware optimization. HLS-derived estimates provide a sufficient baseline for performance comparison, particularly given the infeasibility of manual RTL implementation across the wide array of datasets evaluated in this work.

8. Conclusion

This work shows that Kolmogorov–Arnold Networks (KANs) are uniquely suited to ultrafast on-chip online learning, where MLPs fundamentally struggle. By exploiting B-spline locality, KANs replace dense, interference-prone gradient updates with sparse, targeted coefficient adjustments, while scaling capacity via grid size at near-constant per-sample cost. Additionally, KANs possess theoretical properties that make them inherently robust to fixed-point quantization.

Realized as a custom-hardware FPGA implementation, KANs enable favorable resource scaling and sub-microsecond forward and backward passes with fully on-chip parameter updates, which are three to four orders of magnitude faster than host–accelerator alternatives. Across experiments with drifting regression, adaptive qubit readout, and non-stationary control, KANs consistently outperform parameter-matched MLPs that either diverge under quantization or require impractical precision to stabilize.

More broadly, KANs’ core hardware advantages remain underexplored because modern ML stacks, and GPUs in particular, are built around dense, batched linear algebra rather than localized basis-function learning. Hardware that directly supports spline evaluation and basis selection would make KAN inference and sparse gradient updates hardware-native, enabling ultrafast adaptive control for emerging applications including quantum and plasma systems, networking, and more.

Acknowledgements

DH, AG, and PH are supported by the NSF-funded A3D3 Institute (NSF-PHY-2117997).

Impact Statement

This paper presents work whose goal is to advance the field of Machine Learning. There are many potential societal consequences of our work, none of which we feel must be specifically highlighted here.

References

- Alpaydin, E. and Kaynak, C. Optical Recognition of Handwritten Digits. UCI Machine Learning Repository, 1998. DOI: <https://doi.org/10.24432/C50P49>.
- Babu, P. and Parthasarathy, E. Fpga implementation of multi-dimensional kalman filter for object tracking and motion detection. *Engineering Science and Technology, an International Journal*, 33:101084, 2022. ISSN 2215-0986. doi: <https://doi.org/10.1016/j.jestch.2021.101084>. URL <https://www.sciencedirect.com/science/article/pii/S2215098621002160>.
- Berritta, F., Rasmussen, T., Krzywda, J. A., van der Heijden, J., Fedele, F., Fallahi, S., Gardner, G. C., Manfra, M. J., van Nieuwenburg, E., Danon, J., Chatterjee, A., and Kuemmeth, F. Real-time two-axis control of a spin qubit. *Nature Communications*, 15(1):1676, 2024. doi: [10.1038/s41467-024-45857-0](https://doi.org/10.1038/s41467-024-45857-0). URL <https://doi.org/10.1038/s41467-024-45857-0>.
- Blott, M., Preußer, T. B., Fraser, N. J., Gambardella, G., O'brien, K., Umuroglu, Y., Leeser, M., and Vissers, K. Finn-r: An end-to-end deep-learning framework for fast exploration of quantized neural networks. *ACM Transactions on Reconfigurable Technology and Systems (TRETS)*, 11(3):1–23, 2018.
- Borrageiro, G., Firoozye, N., and Barucca, P. Online learning with radial basis function networks, 2022. URL <https://arxiv.org/abs/2103.08414>.
- Dey, S., Chen, D., Li, Z., Kundu, S., Huang, K.-W., Chugg, K. M., and Beerel, P. A. A highly parallel fpga implementation of sparse neural network training. In *2018 International Conference on ReConfigurable Computing and FPGAs (ReConfig)*, pp. 1–4. IEEE, December 2018. doi: [10.1109/reconfig.2018.8641739](https://doi.org/10.1109/reconfig.2018.8641739). URL <http://dx.doi.org/10.1109/RECONFIG.2018.8641739>.
- Duarte, P. C. L., Dube, A., Zervakis, G., Tahoori, M., and Nassif, S. Function approximation using analog building blocks in flexible electronics, 2025. URL <https://arxiv.org/abs/2502.01489>.
- Fahim, F., Hawks, B., Herwig, C., Hirschauer, J., Jindariani, S., Tran, N., Carloni, L. P., Guglielmo, G. D., Harris, P., Krupa, J., Rankin, D., Valentin, M. B., Hester, J., Luo, Y., Mamish, J., Orgreni-Memik, S., Arrestad, T., Javed, H., Loncar, V., Pierini, M., Pol, A. A., Summers, S., Duarte, J., Hauck, S., Hsu, S.-C., Ngadiuba, J., Liu, M., Hoang, D., Kreinar, E., and Wu, Z. hls4ml: An open-source codesign workflow to empower scientific low-power machine learning devices, 2021. URL <https://arxiv.org/abs/2103.05579>.
- Gadea, R., Cerdà, J., Ballester, F., and Macholi, A. Artificial neural network implementation on a single fpga of a pipelined on-line backpropagation. In *Proceedings 13th International Symposium on System Synthesis*, pp. 225–230, 2000. doi: [10.1109/ISS.2000.874054](https://doi.org/10.1109/ISS.2000.874054).
- Guglielmo, G. D., Du, B., Campos, J., Boltasseva, A., Dixit, A. V., Fahim, F., Kudyshev, Z., Lopez, S., Ma, R., Perdue, G. N., Tran, N., Yesilyurt, O., and Bowring, D. End-to-end workflow for machine learning-based qubit readout with qick and hls4ml, 2025. URL <https://arxiv.org/abs/2501.14663>.
- Hoang, D., Gupta, A., and Harris, P. KANE \acute{E} : Kolmogorov-Arnold Networks for Efficient LUT-based Evaluation. 12 2025. doi: [10.1145/3748173.3779202](https://doi.org/10.1145/3748173.3779202).
- Hooker, S. The hardware lottery, 2020. URL <https://arxiv.org/abs/2009.06489>.
- Hou, Y., Ji, T., Zhang, D., and Stefanidis, A. Kolmogorov-arnold networks: A critical assessment of claims, performance, and practical viability, 2025. URL <https://arxiv.org/abs/2407.11075>.
- Huang, W.-H., Jia, J., Kong, Y., Waqar, F., Wen, T.-H., Chang, M.-F., and Yu, S. Hardware acceleration of kolmogorov-arnold network (kan) for lightweight edge inference. In *Proceedings of the 30th Asia and South Pacific Design Automation Conference, ASPDAC '25*, pp. 693–699, New York, NY, USA, 2025. Association for Computing Machinery. ISBN 9798400706356. doi: [10.1145/3658617.3697677](https://doi.org/10.1145/3658617.3697677). URL <https://doi.org/10.1145/3658617.3697677>.
- Johnson, H., Bornman, N., Kim, T., Zanten, D. V., Zorzetti, S., and Saniie, J. Demonstrating the potential of adaptive lms filtering on fpga-based qubit control platforms for improved qubit readout in 2d and 3d quantum processing units, 2024. URL <https://arxiv.org/abs/2408.00904>.
- Jones, C., Wysocki, P., Feng, M., Paz-Silva, G. A., Ostrove, C. I., Tanttu, T., Rudinger, K. M., Bartee, S. K., Young, K., Hudson, F. E., Lim, W. H., Abrosimov, N. V., Pohl, H.-J., Thewalt, M. L. W., Blume-Kohout, R., Dzurak, A. S.,

- Saraiva, A., Laucht, A., and Yang, C. H. Mid-circuit logic executed in the qubit layer of a quantum processor, 2025. URL <https://arxiv.org/abs/2512.12648>.
- Kara, K., Alistarh, D., Alonso, G., Mutlu, O., and Zhang, C. Fpga-accelerated dense linear machine learning: A precision-convergence trade-off. In *2017 IEEE 25th Annual International Symposium on Field-Programmable Custom Computing Machines (FCCM)*, pp. 160–167, 2017. doi: 10.1109/FCCM.2017.39.
- Konda, V. and Tsitsiklis, J. Actor-critic algorithms. In Solla, S., Leen, T., and Müller, K. (eds.), *Advances in Neural Information Processing Systems*, volume 12. MIT Press, 1999. URL https://proceedings.neurips.cc/paper_files/paper/1999/file/6449f44a102fde848669bdd9eb6b76fa-Paper.pdf.
- Le, L., Kumaraswamy, R., and White, M. Learning sparse representations in reinforcement learning with sparse coding, 2017. URL <https://arxiv.org/abs/1707.08316>.
- Liu, K., Börjeson, E., Häger, C., and Larsson-Edefors, P. Fpga implementation of multi-layer machine learning equalizer with on-chip training. In *2023 Optical Fiber Communications Conference and Exhibition (OFC)*, pp. 1–3, 2023. doi: 10.1364/OFC.2023.M1F.4.
- Liu, Z., Wang, Y., Vaidya, S., Ruehle, F., Halverson, J., Soljačić, M., Hou, T. Y., and Tegmark, M. Kan: Kolmogorov-arnold networks, 2025. URL <https://arxiv.org/abs/2404.19756>.
- Liyanage, N., Wu, Y., Tagare, S., and Zhong, L. Fpga-based distributed union-find decoder for surface codes. *IEEE Transactions on Quantum Engineering*, 5:1–18, 2024. ISSN 2689-1808. doi: 10.1109/tqe.2024.3467271. URL <http://dx.doi.org/10.1109/TQE.2024.3467271>.
- Luo, C., Sit, M.-K., Fan, H., Liu, S., Luk, W., and Guo, C. Towards efficient deep neural network training by fpga-based batch-level parallelism. In *2019 IEEE 27th Annual International Symposium on Field-Programmable Custom Computing Machines (FCCM)*, pp. 45–52, 2019. doi: 10.1109/FCCM.2019.00016.
- Mehrabi, A., Bethi, Y., van Schaik, A., Wabnitz, A., and Afshar, S. Efficient hardware implementation of a multi-layer gradient-free online-trainable spiking neural network on fpga. *IEEE Access*, 12:170980–170993, 2024. ISSN 2169-3536. doi: 10.1109/access.2024.3500134. URL <http://dx.doi.org/10.1109/ACCESS.2024.3500134>.
- Mnih, V., Kavukcuoglu, K., Silver, D., Graves, A., Antonoglou, I., Wierstra, D., and Riedmiller, M. Playing atari with deep reinforcement learning, 2013. URL <https://arxiv.org/abs/1312.5602>.
- Nagabandi, A., Finn, C., and Levine, S. Deep online learning via meta-learning: Continual adaptation for model-based rl, 2019. URL <https://arxiv.org/abs/1812.07671>.
- Reuer, K., Landgraf, J., Fösel, T., O’Sullivan, J., Beltrán, L., Akin, A., Norris, G. J., Remm, A., Kerschbaum, M., Besse, J.-C., Marquardt, F., Wallraff, A., and Eichler, C. Realizing a deep reinforcement learning agent for real-time quantum feedback. *Nature Communications*, 14(1):7138, 2023. doi: 10.1038/s41467-023-42901-3. URL <https://doi.org/10.1038/s41467-023-42901-3>.
- Scheinker, A. Adaptive machine learning for robust diagnostics and control of time-varying particle accelerator components and beams. *Information*, 12(4), 2021. ISSN 2078-2489. doi: 10.3390/info12040161. URL <https://www.mdpi.com/2078-2489/12/4/161>.
- Sivak, V., Morvan, A., Broughton, M., Neeley, M., Eickbusch, A., and et al. Reinforcement learning control of quantum error correction, 2025. URL <https://arxiv.org/abs/2511.08493>.
- Sutton, R. S. Generalization in reinforcement learning: Successful examples using sparse coarse coding. In Touretzky, D., Mozer, M., and Hasselmo, M. (eds.), *Advances in Neural Information Processing Systems*, volume 8. MIT Press, 1995. URL https://proceedings.neurips.cc/paper_files/paper/1995/file/8f1d43620bc6bb580df6e80b0dc05c48-Paper.pdf.
- Tang, Y., Zhang, X., Zhou, P., and Hu, J. Ef-train: Enable efficient on-device cnn training on fpga through data reshaping for online adaptation or personalization, 2022. URL <https://arxiv.org/abs/2202.10935>.
- Tran, V. D., Xuan Hieu Le, T., Tran, T. D., Luan Pham, H., Duong Le, V. T., Hai Vu, T., Nguyen, V. T., and Nakashima, Y. Exploring the limitations of kolmogorov-arnold networks in classification: Insights to software training and hardware implementation. In *2024 Twelfth International Symposium on Computing and Networking Workshops (CANDARW)*, pp. 110–116, 2024. doi: 10.1109/CANDARW64572.2024.00026.
- Venkataramanaiah, S. K., Ma, Y., Yin, S., Nurvithadhi, E., Dasu, A., Cao, Y., and sun Seo, J. Automatic compiler based fpga accelerator for cnn training, 2019. URL <https://arxiv.org/abs/1908.06724>.

Wang, Y., Xu, H., Li, D., Wang, R., Jin, C., Yin, X., Gao, S., Mu, Q., Xuan, L., and Cao, Z. Performance analysis of an adaptive optics system for free-space optics communication through atmospheric turbulence. *Scientific Reports*, 8(1):1124, 2018. doi: 10.1038/s41598-018-19559-9. URL <https://doi.org/10.1038/s41598-018-19559-9>.

Wei, Y., Forelli, R. F., Hansen, C., Levesque, J. P., Tran, N., Agar, J. C., Di Guglielmo, G., Mauel, M. E., and Navratil, G. A. Low latency optical-based mode tracking with machine learning deployed on fpgas on a tokamak. *Review of Scientific Instruments*, 95(7), July 2024. ISSN 1089-7623. doi: 10.1063/5.0190354. URL <http://dx.doi.org/10.1063/5.0190354>.

Yan, F., Koch, A., and Sinnen, O. A survey on fpga-based accelerator for ml models, 2024. URL <https://arxiv.org/abs/2412.15666>.

Zang, Z., Li, X., and Li, D. D. U. Online learning extreme learning machine with low-complexity predictive plasticity rule and fpga implementation, 2025. URL <https://arxiv.org/abs/2512.21777>.

Zhang, K., Hawkins, C., Zhang, X., Hao, C., and Zhang, Z. On-fpga training with ultra memory reduction: A low-precision tensor method, 2021. URL <https://arxiv.org/abs/2104.03420>.

A. Theorem Proofs

A.1. Proof of Theorem 3.3 (Update Complexity)

Setup: Let the total parameter budget be N . We compare a standard MLP layer with input dimension d_{in} and output dimension d_{out} against a KAN layer with identical input/output dimensions. Let s denote the B-spline support size (order $p+1$) and G denote the grid size. For the KAN layer, the total number of parameters is $N_{\text{KAN}} = d_{\text{in}}d_{\text{out}}(G+s)$. To maintain the fixed budget N , we assume $d_{\text{in}}d_{\text{out}} = N/(G+s)$.

Proof. We analyze the scalar arithmetic operations required to compute the gradient with respect to the weights for a single sample (x, y) . Let $\delta \in \mathbb{R}^{d_{\text{out}}}$ be the backpropagated error signal (gradient of loss w.r.t layer output).

Case 1: MLP Update Complexity. The gradient update for an MLP weight matrix $W \in \mathbb{R}^{d_{\text{out}} \times d_{\text{in}}}$ is given by the outer product:

$$\nabla_W \mathcal{L} = \delta x^\top$$

For each element $W_{j,i}$, the computation requires 1 multiplication. The total number of update operations is:

$$\mathcal{C}_{\text{MLP}} = d_{\text{in}}d_{\text{out}} = N_{\text{MLP}} = N$$

Case 2: KAN Update Complexity. The KAN layer output is $y_j = \sum_{i=1}^{d_{\text{in}}} \sum_{g=1}^G w_{j,i,g} B_g(x_i)$. The gradient with respect to a specific spline coefficient $w_{j,i,g}$ is:

$$\frac{\partial \mathcal{L}}{\partial w_{j,i,g}} = \frac{\partial \mathcal{L}}{\partial y_j} \frac{\partial y_j}{\partial w_{j,i,g}} = \delta_j B_g(x_i)$$

Due to the local support property of B-splines (Lemma 3.2), for a given input coordinate x_i , $B_g(x_i)$ is nonzero for at most s indices. Let $\mathcal{K}_i = \{g \mid B_g(x_i) \neq 0\}$ be the set of active indices for input i , where $|\mathcal{K}_i| \leq s$. The gradient is zero for all $g \notin \mathcal{K}_i$. Therefore, we only perform updates for indices in \mathcal{K}_i .

The total number of operations is the sum of updates over all edges (i, j) :

$$\mathcal{C}_{\text{KAN}} = \sum_{j=1}^{d_{\text{out}}} \sum_{i=1}^{d_{\text{in}}} |\mathcal{K}_i| \leq d_{\text{out}}d_{\text{in}}s$$

Substituting the parameter count relationship $d_{\text{in}}d_{\text{out}} = P/(G+s)$:

$$\mathcal{C}_{\text{KAN}} \leq \frac{N}{G+s} \cdot s = N \left(\frac{s}{G+s} \right)$$

Conclusion. Comparing the two complexities:

$$\frac{\mathcal{C}_{\text{KAN}}}{\mathcal{C}_{\text{MLP}}} = \frac{N(s/(G+s))}{N} = \frac{s}{G+s}$$

Since s is fixed (typically 3 or 4) and G scales with grid resolution (typically $G \gg s$), the KAN update complexity is strictly sublinear relative to the parameter budget. \square

A.2. Proof of Theorem 3.4 (KAN Activation Bounds)

Proof. Let $m = \min_g W_g$ and $M = \max_g W_g$. For normalized B-splines, we have for any x in the domain:

$$B_g(x) \geq 0 \quad \text{and} \quad \sum_g B_g(x) = 1.$$

Consider

$$\phi(x) = \sum_g W_g B_g(x).$$

Using the partition of unity,

$$\phi(x) - m = \sum_g W_g B_g(x) - m \sum_g B_g(x) = \sum_g (W_g - m) B_g(x) \geq 0,$$

since $W_g - m \geq 0$ and $B_g(x) \geq 0$. Thus $\phi(x) \geq m$.

Similarly,

$$M - \phi(x) = \sum_g M B_g(x) - \sum_g W_g B_g(x) = \sum_g (M - W_g) B_g(x) \geq 0,$$

so $\phi(x) \leq M$.

Hence,

$$\min_g W_g \leq \phi(x) \leq \max_g W_g.$$

□

A.3. Proof of Theorem 3.5 (Bounded Gradient Sensitivity)

Proof. We examine the gradient of the loss \mathcal{L} with respect to parameters in a single layer ℓ , considering a connection from input node i to output node j . Let $\delta_{\ell+1,j} = \frac{\partial \mathcal{L}}{\partial x_{\ell+1,j}}$ denote the backpropagated error signal.

Case 1: MLP. The pre-activation output is

$$x_{\ell+1,j} = \sum_{i=1}^{d_{\text{in}}} W_{\ell,ji} x_{\ell,i}.$$

By the chain rule, the gradient with respect to $W_{\ell,ji}$ is

$$\frac{\partial \mathcal{L}}{\partial W_{\ell,ji}} = \delta_{\ell+1,j} \cdot \frac{\partial x_{\ell+1,j}}{\partial W_{\ell,ji}} = \delta_{\ell+1,j} \cdot x_{\ell,i}.$$

Under quantization, input perturbations ξ with $|\xi| = O(\Delta)$ induce gradient error proportional to $|\delta_{\ell+1,j}| \cdot |\xi|$. Critically, the gradient magnitude itself scales with $|x_{\ell,i}|$, coupling the update dynamic range to the input distribution.

Case 2: KAN. The layer output is

$$x_{\ell+1,j} = \sum_{i=1}^{n_{\ell}} \phi_{\ell,j,i}(x_{\ell,i}) = \sum_{i=1}^{n_{\ell}} \sum_{g=1}^G w_{\ell,j,i,g} B_g(x_{\ell,i}).$$

The gradient with respect to coefficient $w_{\ell,j,i,g}$ is

$$\frac{\partial \mathcal{L}}{\partial w_{\ell,j,i,g}} = \delta_{\ell+1,j} \cdot \frac{\partial x_{\ell+1,j}}{\partial w_{\ell,j,i,g}} = \delta_{\ell+1,j} \cdot B_g(x_{\ell,i}).$$

By the partition of unity property of B-splines, $\sum_g B_g(x) = 1$ and $0 \leq B_g(x) \leq 1$ for all x and g . Therefore,

$$\left| \frac{\partial \mathcal{L}}{\partial w_{\ell,j,i,g}} \right| = |\delta_{\ell+1,j}| \cdot |B_g(x_{\ell,i})| \leq |\delta_{\ell+1,j}|.$$

Unlike the MLP case, the factor multiplying the error signal is structurally bounded to $[0, 1]$, decoupling the gradient dynamic range from the input magnitude $|x_{\ell,i}|$.

Quantization Error Variance. For MLPs, quantization noise $\xi \sim O(\Delta)$ in $x_{\ell,i}$ produces gradient error with variance

$$\text{Var}[\epsilon_{\text{MLP}}] \propto \mathbb{E}[\delta_{\ell+1,j}^2] \cdot \text{Var}[\xi] = O(\Delta^2 \text{Var}[x_{\ell}]).$$

For KANs, since $B_g(x_{\ell,i}) \in [0, 1]$ regardless of $x_{\ell,i}$, the gradient error variance satisfies

$$\text{Var}[\epsilon_{\text{KAN}}] \leq \mathbb{E}[\delta_{\ell+1,j}^2] \cdot O(\Delta^2) = O(\Delta^2),$$

which is independent of input statistics. □

B. FPGA Implementation Details

B.1. Code generation and build flow

We generate one self-contained Vitis HLS project per model configuration. A lightweight Python frontend writes a set of C++ headers/sources from templates: (i) `defines.h` (dimensions, precisions, grid constants, learning rate), (ii) `parameters.h` (parameter and context structs, plus parameter initialization), (iii) `components.h` (layer primitives: forward/backward/update), and (iv) a top-level kernel (`kan.cpp` / `mlp.cpp`) that invokes all layers in sequence. A `build.tcl` script specifies the target FPGA part and clock period for Vitis HLS synthesis.

B.2. Fixed-point formats and saturation

All arithmetic uses either `ap_fixed<W,I>` with rounding and saturation (AP_RND_CONV, AP_SAT) or IEEE float (for ablations). The float datatype is used only to study convergence behavior, not for hardware analysis. We define three independent types: `input_t` for inputs, `weight_t` for parameters/accumulators, and `output_t` for outputs/feedback. The learning rate is compiled as a constant of type `weight_t`.

B.3. KAN layer implementation

Uniform grid and indexing. Let the grid cover $[x_{\min}, x_{\max}]$ with G cells of width $H = (x_{\max} - x_{\min})/G$. For each coordinate x , we compute $t = (x - x_{\min})/H$, clamp t to $[0, G]$, and set $k = \lfloor t \rfloor$ (cell index). Within the cell, we use a small fractional index u obtained from the low bits of a fixed-point representation of t , producing `LUT_RESOLUTION` = 2^F bins per cell. We store (k, u) for each (o, i) pair in a per-layer context to make the backward pass purely index-driven.

Basis LUTs (values and derivatives). For spline order p , at most $s = p + 1$ basis functions are nonzero per cell. We precompute a constant LUT:

$$\text{LUT.B}_r[u] \approx B_r(\xi_u), \quad \text{LUT.dB}_r[u] \approx \frac{d}{dx} B_r(\xi_u),$$

for $r = 0, \dots, p$ and $u = 0, \dots, 2^F - 1$, where ξ_u are uniformly spaced sample points over a unit cell. F is a hyperparameter for how many bits are used to address `LUT.Br[u]` and is specified in the user-defined configuration. The LUT is compiled into `parameters.h` as a read-only constant and bound to on-chip ROM (LUTRAM).

Forward pass (KAN). Each layer stores parameters as `Ws[o][i][c]` with coefficient index $c \in \{0, \dots, (G+p-1)\}$. Given (k, u) for input x_i , we evaluate only the active coefficients:

$$\phi_{o,i}(x_i) \approx \sum_{r=0}^p \text{Ws}[o][i][k+r] \cdot \text{LUT.B}_r[u], \quad y_o = \sum_i \phi_{o,i}(x_i).$$

In hardware, the inner sums are fully unrolled across r and typically across i (subject to resource constraints), with a final unrolled reduction over i .

Backward pass and in-place update (KAN). For the upstream gradient $g_o = dL/dy_o$, the coefficient update for the active cell is

$$\text{Ws}[o][i][k+r] \leftarrow \text{Ws}[o][i][k+r] - \eta g_o \text{LUT.B}_r[u], \quad r = 0, \dots, p.$$

The downstream gradient for each input coordinate is computed via LUT derivatives:

$$\frac{dL}{dx_i} = \sum_o g_o \sum_{r=0}^p \text{Ws}[o][i][k+r] \cdot \text{LUT.dB}_r[u].$$

In the implementation, (k, u) are read from context, the r -loop is unrolled, and dL/dx_i is accumulated across o .

B.4. MLP baseline implementation

Forward. Each layer computes $z_o = \sum_i W[o][i]x_i + b[o]$ and applies a hardware-friendly activation. In our experiments, we use ReLU; we also support piecewise `hard_tanh` and `hard_silu` variants. For backprop, we store in context: (i) a copy of the layer input x and (ii) the pre-activation vector z (except for the final linear layer).

Backward and update. Given upstream gradient dL/dy , we compute $dL/dz = (dL/dy) \odot f'(z)$ for hidden layers (and $dL/dz = dL/dy$ for the linear output layer), then apply in-place SGD updates:

$$b[o] \leftarrow b[o] - \eta dL/dz_o, \quad W[o][i] \leftarrow W[o][i] - \eta dL/dz_o x_i.$$

The downstream gradient is

$$\frac{dL}{dx_i} = \sum_o (dL/dz_o) W_{\text{old}}[o][i],$$

where we use W_{old} (the weight prior to update) to match standard backprop ordering.

Initialization and parity with PyTorch. Weights and biases are initialized with the same per-layer scale as common PyTorch uniform schemes (using a scale proportional to $1/\sqrt{d_{\text{in}}}$) to ensure controlled comparisons.

B.5. HLS directives and on-chip storage

Deterministic control. All loops have static bounds determined by compile-time dimensions. The kernels are structured to enable deterministic scheduling: unrolled inner loops for parallel MACs/coefficients updates and pipelining across output neurons where appropriate.

LUT storage. KAN basis/derivative LUTs are bound to single-port ROM implemented in LUTRAM (read-only, constant at synthesis), minimizing BRAM pressure.

Parameter storage. KAN parameters are stored as a 3D array $W_s[o][i][c]$. We apply complete partitioning across o and i , and cyclic partitioning across the coefficient dimension c with factor $(p+1)$ to match the number of active basis functions per cell. MLP weights $W[o][i]$ and biases $b[o]$ are partitioned to expose full parallelism across dot-products and updates. Per-layer contexts (KAN indices; MLP cached x and z) are fully partitioned and reside in registers/small RAMs.

B.6. Software Interface and Verification

CPU-loadable functional model. For rapid functional testing and simulation of fixed-point arithmetic, we compile the generated HLS C++ into a CPU-loadable shared library and invoke it from Python via `ctypes`. The exposed interface accepts pointers to the input, output, and feedback tensors, together with a `zero_grad` flag controlling whether parameter updates are applied. This setup enables fast iteration and direct comparison against software reference implementations without FPGA synthesis.

Functional verification. We use the shared library to validate both numerical correctness and learning dynamics. For each architecture, we first verify convergence behavior in floating-point mode using HLS emulation. In this setting, the HLS MLP implementation matches an equivalent PyTorch model exactly, including initialization and update ordering, providing a strong software reference. All fixed-point experiments are then performed with identical architectures and learning rules, ensuring that any observed differences arise solely from quantization and hardware execution effects.

B.7. HLS Synthesis

The verified HLS designs are synthesized using Vitis HLS via an automatically generated `build.tcl` script. Synthesis reports provide estimates of kernel latency, initiation interval, and on-chip resource utilization (LUTs, DSPs, BRAMs). Unless otherwise stated, all designs target an AMD Virtex™ UltraScale+™ XCVU13P FPGA and are synthesized with a target clock period of 5 ns (200 MHz). All comparisons between KAN and MLP implementations are performed under identical timing, precision, and synthesis constraints.

C. Benchmark 2 Details: Adaptive Single-shot Qubit Readout

We instantiate adaptive single-shot readout as a *fully online* binary classification problem on streaming IQ samples. At each time step t , the learner receives a single point $\mathbf{x}_t = (I_t, Q_t) \in \mathbb{R}^2$, predicts $\hat{y}_t \in \{-1, +1\}$, and immediately receives the true label $y_t \in \{-1, +1\}$ and updates once. The data distribution drifts continuously in time and is intentionally non-linearly separable due to a Kerr-type phase distortion.

Algorithm 1 Rotating XOR stream with Kerr distortion

-
- 1: Sample latent index $s \sim \text{Unif}\{0, 1, 2, 3\}$ and set label $y \in \{-1, +1\}$ by parity.
 - 2: Set center $\mu_s \in \mathbb{R}^2$ from the quadrant list.
 - 3: Sample $(I, Q) \sim \mathcal{N}(\mu_s, \sigma^2 \mathbf{I}_2)$.
 - 4: Compute $r = \sqrt{I^2 + Q^2}$, $\phi = \text{atan2}(Q, I)$, and apply Kerr twist $\phi \leftarrow \phi + \kappa r^2$.
 - 5: Set $(I, Q) \leftarrow (r \cos \phi, r \sin \phi)$.
 - 6: Apply breathing $(I, Q) \leftarrow p_t(I, Q)$ with $p_t = 1 + a \sin(\omega t)$.
 - 7: Rotate by $\theta_t = \text{rad}(t \cdot \text{drift_speed})$: $(I, Q) \leftarrow R(\theta_t)(I, Q)$.
- output** $\mathbf{x}_t = (I, Q)$ and $y_t = y$.
-

C.1. Rotating XOR constellation with Kerr distortion and drift

Latent state and class definition. Each sample is generated by first drawing a latent ‘‘computational-basis’’ index

$$s_t \sim \text{Unif}\{0, 1, 2, 3\},$$

corresponding to one of four Gaussian blobs centered in the four quadrants of the IQ plane. We use an XOR/parity labeling:

$$y_t = \begin{cases} -1, & s_t \in \{0, 1\} \quad (\text{quadrants 1 \& 3}) \\ +1, & s_t \in \{2, 3\} \quad (\text{quadrants 2 \& 4}). \end{cases}$$

This creates the classic 2D XOR decision boundary (non-linearly separable).

Base blob centers and noise. Let $\text{spread} > 0$ set the separation between blob centers and $\sigma > 0$ set isotropic Gaussian noise. We define the unrotated centers

$$\begin{aligned} \mu_0 &= (+\text{spread}, +\text{spread}), & \mu_1 &= (-\text{spread}, -\text{spread}), \\ \mu_2 &= (-\text{spread}, +\text{spread}), & \mu_3 &= (+\text{spread}, -\text{spread}). \end{aligned}$$

then sample

$$(I, Q) \sim \mathcal{N}(\mu_{s_t}, \sigma^2 \mathbf{I}_2).$$

Kerr-type phase distortion. To emulate non-linear IQ warping (e.g. due to Kerr physics), we apply a phase twist that grows with amplitude. Let $r = \sqrt{I^2 + Q^2}$ and $\phi = \text{atan2}(Q, I)$. We compute

$$\phi' = \phi + \kappa r^2, \quad (I, Q) \leftarrow (r \cos \phi', r \sin \phi'),$$

where κ controls distortion strength. This transforms circular blobs into ‘‘comet-shaped’’ clusters and makes simple linear or distance-based boundaries suboptimal.

Slow drift: global rotation and breathing. We impose two forms of non-stationarity.

(i) *Global rotation.* At time t , we rotate the entire constellation by angle

$$\theta_t = \text{rad}(t \cdot \text{drift_speed}),$$

where $\text{rad}(\cdot)$ converts degrees to radians (matching the implementation). We then apply

$$\begin{bmatrix} I \\ Q \end{bmatrix} \leftarrow \begin{bmatrix} \cos \theta_t & -\sin \theta_t \\ \sin \theta_t & \cos \theta_t \end{bmatrix} \begin{bmatrix} I \\ Q \end{bmatrix}.$$

(ii) *Breathing/pulsing.* We optionally modulate the radius by a slow sinusoid

$$(I, Q) \leftarrow p_t(I, Q), \quad p_t = 1 + a \sin(\omega t),$$

which induces gradual expansion/contraction and further stresses online adaptation.

Table 2. Default stream parameters for Benchmark 2 (matching the code).

Parameter	Symbol	Value
Blob separation	spread	1.5
Gaussian noise std.	σ (noise_scale)	0.4
Kerr distortion strength	κ (kerr_strength)	0.4
Rotation rate (deg/step)	drift_speed	0.05
Breathing amplitude	a	0.2
Breathing frequency	ω	0.01

C.2. Reference implementation and hyperparameters

Algorithm 1 summarizes the generator used in our experiments. Unless stated otherwise, we use the default parameters in Table 2, which match the provided code.

C.3. Online protocol and reported metric

At each step t , the learner: (i) observes \mathbf{x}_t , (ii) outputs $\hat{y}_t \in \{-1, +1\}$, (iii) receives y_t immediately, and (iv) performs a single gradient update using only the current sample (no replay/buffering). We report *instantaneous accuracy* $\mathbf{1}\{\hat{y}_t = y_t\}$ and its running mean over time (the plotted “running accuracy”). When visualizing decision boundaries (Fig. 6), we freeze model parameters at the indicated time and evaluate \hat{y} on a dense grid in the (I, Q) plane.

Reproducibility. All results are generated using the same streaming procedure described above, with fixed seeds per run. When sweeping capacity (KAN grid size G or MLP parameter count N), we keep the stream parameters fixed (Table 2) and vary only model/hardware configurations.